

Detection of flare multi-periodic pulsations in mid-ultraviolet Balmer continuum, Ly α , hard X-ray, and radio emissions simultaneously

Dong Li^{1,2}, Mingyu Ge³, Marie Dominique⁴, Haisheng Zhao³, Gang Li³, Xiaobo Li³, Shuangnan Zhang^{3,5}, Fangjun Lu³, Weiqun Gan^{1,6}, and Zongjun Ning^{1,6}

¹*Key Laboratory of Dark Matter and Space Astronomy, Purple Mountain Observatory, CAS, Nanjing 210023, PR China*

²*State Key Laboratory of Space Weather, Chinese Academy of Sciences, Beijing 100190, PR China*

³*Key Laboratory of Particle Astrophysics, Institute of High Energy Physics, Chinese Academy of Sciences, Beijing 100049, PR China*

⁴*Solar-Terrestrial Centre of Excellence/SIDC, Royal Observatory of Belgium, 3 Avenue Circulaire, B-1180 Uccle, Belgium*

⁵*University of Chinese Academy of Sciences, Chinese Academy of Sciences, Beijing 100049, PR China*

⁶*School of Astronomy and Space Science, University of Science and Technology of China, Hefei 230026, PR China*

ABSTRACT

Quasi-periodic pulsations (QPPs), which usually appear as temporal pulsations of the total flux, are frequently detected in the light curves of solar/stellar flares. In this study, we present the investigation of non-stationary QPPs with multiple periods during the impulsive phase of a powerful flare on 2017 September 06, which were simultaneously measured by the Large-Yield Radiometer (LYRA) and the Hard X-ray Modulation Telescope (Insight-HXMT), as well as the ground-based BLENSSW. The multiple periods, detected by applying a wavelet transform and Lomb-Scargle periodogram to the detrended light curves, are found to be $\sim 20\text{--}55$ s in the Ly α and mid-ultraviolet Balmer continuum emissions during the flare impulsive phase. Similar QPPs with multiple periods are also found in the hard X-ray emission and low-frequency radio emission. Our observations suggest that the flare QPPs could be related to nonthermal electrons accelerated by the repeated energy release process, i.e., triggering of repetitive magnetic reconnection, while the multiple periods might be modulated by the sausage oscillation of hot plasma loops. For the multi-periodic pulsations, other generation mechanisms could not be completely ruled out.

Subject headings: Solar flares — Solar oscillations — Solar ultraviolet emission — Solar X-ray emission — Solar radio emission

1. Introduction

Solar flares are powerful eruption events on the Sun associated with a rapid and violent release of magnetic free energy through a reconnection process. A typical flare can radiate at almost all wavelengths constituting the solar spectrum, ranging from radio through optical and ultraviolet (UV) to soft/hard X-ray (SXR/HXR) and even γ -rays (e.g., Benz 2017; Tan et al. 2020). Only a small part of the flare radiation is emitted at the shortest wavelengths in the X-ray and extreme UV (EUV) ranges (Emslie et al. 2012). The quantitative estimation of the radiated flare energy partition suggested that about 70% in white light (WL) for solar flares (e.g., Kretzschmar 2011) and 55%–80% in WL for stellar flares (e.g., Kuznetsov & Kolotkov 2021). In other words, most of the flare energy is radiated in the longer wavelengths (Kleint et al. 2016). Between those extremes, the solar UV spectrum from 1000 Å to 3000 Å, which can be further split into the far-ultraviolet (FUV), the mid-ultraviolet (MUV), and the near-ultraviolet (NUV), is thought to provide an important contribution to the flare radiation (Woods et al. 2006; Milligan et al. 2014; Dominique et al. 2018). For instance, the Ly α spectral line produced by the chromospheric neutral hydrogen, which is centered at 1216 Å (in the FUV spectrum), is among the spectral lines in which flares radiate the most (Allred et al. 2005; Curdt et al. 2001; Lu et al. 2021a). The hydrogen Balmer continuum emitted during flares, which is thought to be generated during the recombination of flare-produced free electrons in the chromosphere, is often detected in the MUV and NUV ranges, as well as close to the Balmer recombination edge at 3646 Å (Heinzel & Kleint 2014; Kotrč et al. 2016; Dominique et al. 2018). Both the Ly α and hydrogen Balmer continuum emissions during solar flares are expected to be nonthermal profiles, i.e., similar to the HXR radiation which is produced by the beam of electrons that are accelerated by the magnetic reconnection during the solar flare (e.g., Avrett et al. 1986; Rubio da Costa et al. 2009; Heinzel & Kleint 2014).

Quasi-periodic pulsations (QPPs) often refer to the quasi-periodic intensity variations during solar/stellar flares (see Zimovets et al. 2021, for a recent review). In many observations, the flare QPPs were found to show a non-stationary property in the time series integrated over the whole Sun/star or over the oscillation region, for instance, each pulsation has an anharmonic and symmetric triangular profile shape (e.g., Kolotkov et al. 2015; Nakariakov et al. 2019). The signature of flare QPPs can be detected in flare light curves across a broad band of the electromagnetic spectrum, i.e., radio/microwave emissions (Ning et al. 2005; Reznikova & Shibasaki 2011; Nakariakov et al. 2018; Yu & Chen 2019), UV/EUV wavelengths (Shen et al. 2018; Hayes et al. 2019; Reeves et al. 2020; Miao et al. 2021), SXR/HXR and γ -rays channels (Nakariakov et al. 2010; Ning 2017; Hayes et al. 2020; Li et al. 2020a), as well as the H α (Srivastava et al. 2008; Kashapova et al. 2020; Li et al. 2020b) or Ly α (Van Doorselaere et al. 2011; Milligan et al. 2017; Li 2021) emissions. The quasi-periods of these QPPs were reported from sub-seconds to tens of minutes (e.g., Tan et al. 2010; Shen et al. 2013, 2019; Kolotkov et al. 2018; Karlický & Rybák 2020; Clarke et al. 2021). It should be stated that the observed periods are generally related to the specific channels or flare phases (Tian et al. 2016; Dennis et al. 2017; Pugh et al. 2019), suggesting that the various classes of QPPs could be produced by different generation mechanisms

(e.g., Kupriyanova et al. 2020). In the literature, the flare-related QPPs were most often explained by magnetohydrodynamic (MHD) waves, more specifically, sausage waves, kink waves, and slow waves (Li et al. 2020c; Nakariakov & Kolotkov 2020; Wang et al. 2021), or by a repetitive regime of magnetic reconnection that could be spontaneous (i.e., self-oscillatory process) or triggered due to external MHD oscillations (Thurgood et al. 2017; Yuan et al. 2019; Clarke et al. 2021). They can also be interpreted in terms of the LRC-circuit oscillation in current-carrying loops (Tan et al. 2016; Li et al. 2020b) or caused by the interaction between supra-arcade downflows and flare loops (Xue et al. 2020; Samanta et al. 2021).

The hydrogen Balmer continuum enhancement at MUV wavelengths around 2000 Å was found to be highly synchronous with the enhancement of Ly α emission during a powerful solar flare (Dominique et al. 2018), while the flare radiation in the Ly α and HXR ranges were demonstrated to have a close relationship (Nusinov et al. 2006; Jing et al. 2020; Lu et al. 2021b). However, flare-related QPPs were rarely observed simultaneously in these channels. In this study, we report the detection of flare-related QPPs with multi-periodicity in the MUV Balmer continuum, Ly α , HXR and radio emissions during the impulsive phase of a powerful solar flare.

2. Observations and Instruments

On 2017 September 06, the active region of NOAA 12673 produced the most powerful flare of the solar cycle 24, measured to be of the X9.3 class. It was simultaneously recorded by the space-based instruments of Large-Yield RAdiometer (LYRA) on board the PRoject for OnBoard Autonomy 2 (PROBA2) mission (Dominique et al. 2013), the Hard X-ray Modulation Telescope (Insight-HXMT) (Zhang et al. 2020), and the Geostationary Operational Environmental Satellite 16 (GOES-16), as well as the ground-based CALLISTO radio spectrograph (Benz et al. 2009) at BLENSW, as shown in Figure 1 and table 1. Note that all the space- and ground-based instruments observe in a Sun-as-a-star mode. The GOES SXR flux at 1–8 Å (black curve) suggests that the powerful flare begins at about 11:53 UT and reaches its maximum at around 12:02 UT¹, as indicated by the vertical dashed line in Figure 1 (a).

LYRA provides the solar irradiance measurement in four wide spectral channels with a high time resolution of 0.05 s (Dominique et al. 2013, 2018). Channels 3 and 4 measure the solar radiation in SXR/EUV ranges at 1–800 Å and 1–200 Å, and they look very similar. Therefore, only the light curve from channel 4 (blue) is shown in Figure 1 (a), which exhibits a similar time evolution as the GOES SXR flux. However, the flux peak is a bit later than that of the GOES SXR flux. This could be attributed to the observational fact that the light curve from LYRA channel 4 measures the solar SXR/EUV radiation in a long and broad wavelength range, i. e., 1–200 Å (Dominique et al. 2018), while the GOES SXR flux only covers a short and narrow wavelength

¹<https://www.solarmonitor.org/?date=20170906>

range of 1–8 Å. On the other hand, the channel 1 observes the solar irradiance in the FUV channel centered at the Ly α 1216 Å line, which is also referred to as the Ly α channel. While the channel 2 takes the solar observation in the MUV channel between 1900 Å and 2220 Å, which is demonstrated to be consistent with the hydrogen Balmer continuum emission around 2000 Å, and is formed in the chromosphere (e.g., Dominique et al. 2018). Therefore, the LYRA channel 2 is considered to provide the solar radiation in the MUV Balmer continuum. Figure 1 (b) draws the normalized light curves between 11:55:07 UT and 12:03:27 UT from LYRA channels in the Ly α (black) and MUV Balmer continuum (cyan) ranges, showing a well synchronous relationship in the time series. Taking into account that LYRA observes in a Sun-as-a-star mode, it is impossible to conclude that they are radiated from a same source area, due to the lack of the spatially resolved information.

In this study, two X-ray light curves measured by the Insight-HXMT (Zhang et al. 2020), which has a time cadence of 1 s, were also used to investigate the flare-related QPPs. The Medium Energy X-ray telescope (ME) observes the X-ray emission normally at 5–30 keV (Cao et al. 2020; Luo et al. 2020). The Anti-Coincidence Detectors (ACD) provides the HXR flux at higher energy, i.e., >100 keV, which was adopted from the High Energy X-ray telescope after removing the background that is induced by the particle (Liu et al. 2020). Figure 1 (b) presents the X-ray light curves as normalization during 11:55:07–12:03:27 UT derived from the ME (magenta) and ACD (red). They both match well with the LYRA light curves at channels 1 and 2, but the ACD light curve seems to show a much clear enhancement after 12:00 UT, as indicated by the red arrow. Moreover, there is almost no time delay between the light curves measured by the LYRA and the Insight-HXMT, both of which have very burst profiles, confirming their nonthermal profiles.

The major X9.3 flare was also observed by the radio spectrogram from the BLENSSW (Benz et al. 2009) at low frequencies between about 20 MHz and 76 MHz, which has a time cadence of 0.25 s, as shown by the context image in Figure 1 (a) and table 1. A sequence of transient bursts can be found in the radio dynamic spectrum during the flare impulsive phase, i. e., during \sim 11:57–12:02 UT. They all drift rapidly from high to low frequencies over a quite short time, which can be regarded as the type III radio bursts and could be helpful to trace the propagating electron beams through the solar atmosphere during solar flares. Figure 1 (b) also draws the normalized radio flux (green) at a low frequency of 34.75 MHz, which has been shifted in height to show clearly. It exhibits a burst profile, which is similar to the light curves recorded by the LYRA and the Insight-HXMT. Obviously, the onset time of the enhancement in radio flux at the low frequency is later than that in light curves at Ly α , MUV Balmer continuum and HXR emissions.

3. Results

The flare light curves at wavelengths of MUV Balmer continuum, Ly α , and HXR are characterized by a number of small pulsations, referred to as QPPs. Similar to previous observations (Ning 2014; Li et al. 2017; Milligan et al. 2017; Feng et al. 2020), these small pulsations superimposed on the strong background. To look more closely at the periodicity of this flare, we apply the wavelet

transform method (Torrence & Compo 1998) to the detrended light curves, where detrending is obtained by filtering out the longest periods (i.e., the long-term trend) from the original/raw time series. Here, the wavelet mother function of ‘Morlet’ is used for the wavelet analysis. The results are shown in Figures 2, 4 and 5. Based on the fast Fourier transform (FFT) method, the raw light curves measured by LYRA, Insight-HXMT, and BLENSSW are detrended using a cutoff threshold of 60 s, thereby enhancing the periods that are shorter than 60 s. Thus, the periodic features with short periods can be highlighted in the wavelet power spectrum (Feng et al. 2017; Ning 2017; Milligan et al. 2017).

Figure 2 presents the Morlet wavelet analysis results for the LYRA data from two channels. The top two panels draw the raw light curves of $\text{Ly}\alpha$ (channel 1) and MUV Balmer continuum (channel 2) emissions, the long-term trend obtained by FFT-filtering are overplotted in green. Two main pulses appear in the raw light curves during about 11:55:40–11:58:20 UT, as indicated by the two green arrows in panels (a) & (d). The oscillatory amplitude of the two main pulses is much larger than that of the short-period QPPs studied in this study, which may result in a weak power of the wavelet analysis. Therefore, to suppress the long-period trend that is caused by the two main pulses, a cutoff period of ~ 60 s is used to the raw light curves. The detrended light curves are obtained by subtracting the FFT filtered time series, as plotted in the middle panels. They both show a series of pulsations, and each pulsation has an anharmonic and symmetric triangular profile shape, which can be regarded as the signature of non-stationary QPPs. The bottom panels plot the wavelet power spectra for the detrended light curves in $\text{Ly}\alpha$ (c) and MUV Balmer continuum (f) emissions, both of which show an enhanced power over a wide range of periods during the impulsive phase of the powerful flare, i.e., between about 11:56 UT and 12:02 UT, implying the multi-periodicity QPPs. The bulk of the detections in the two power spectra are evident at periods of about 20–55 s. Interestingly, the quasi-periods appear to have different lifetimes. For instance, the quasi-periods of ~ 20 –30 s are seen to happen from about 11:56 UT to 11:57 UT only, while the 30–50 s QPPs are seen to occur between about 11:56 UT and 11:59 UT, and the quasi-periods of 50–55 s are seen to appear during $\sim 11:57$ –12:02 UT. However, the 50–55 s QPP signal is very close to the cutoff threshold, which might be an artefact of detrending. Similarly to previous studies (Kupriyanova et al. 2010; Milligan et al. 2017), we then extracted the detrended time series from the raw LYRA data with a long cutoff threshold of 120 s, as shown in Figure A. The wavelet power spectra show a much broader range of periods, such as 20–100 s. The strongest power appears at the periods of ~ 60 –100 s between $\sim 11:55:40$ UT and $\sim 11:58:20$ UT, which is largely due to the two main pulses shown by the green arrows in Figure 2 (a) and (d). They are not suppressed when we used a cutoff threshold of 120 s for detrending, as shown in Figure A (a) & (b). On the other hand, the short periods of about 20–55 s exhibits a little weak power, but they are still inside the 99.9% significance level, which confirms that the short periods in LYRA channels 1 and 2 are not artifacts of the detrending process.

The wavelet power spectra in Figure A show a broad range of periods with a brightest core and weaker borders. Using the Lomb-Scargle periodogram method (Scargle 1982), the periodogram

analysis is performed to the detrended light curves. Figure 3 presents the normalized FFT power spectra at LYRA channels 1 (a) and 2 (b), and two different values of cutoff thresholds are used for detrending, e.g., 60 s (black) and 120 s (magenta), respectively. The dashed lines in the FFT spectra represent the significance levels of 99.9%, which are estimated from the red noise in quasi-periodic signals (Vaughan 2005; Liang et al. 2020; Anfinogentov et al. 2021). The short periods of $\sim 20\text{--}55$ s can be simultaneously seen in all the FFT power spectra, but the quasi-periods of $\sim 20\text{--}40$ s are quite weak in the FFT power spectra from the detrending light curves by applying a big cutoff threshold of 120 s, as shown by the magenta lines. On the other hand, the long period of roughly 80 s is only found in the FFT power spectra from the detrending light curves by applying the 120-s cutoff threshold, and it is well suppressed by the 60-s cutoff threshold, which is similar to Morlet wavelet analysis results. The FFT spectra further confirm that the short periods of $\sim 20\text{--}55$ s are not artifacts of the detrending process. However, it is impossible to determine the duration of the short periods, especially the lifetime of periods between 50–55 s, since they are also seen at the border edges of the strongest power in the wavelet power spectra in Figure A. We also notice that the 80-s period has been studied in the flare emission at wavelengths of Ly α (Li et al. 2020d) and HXR emission (Zhang et al. 2021), respectively. Therefore, we only focused on the short periods of $\sim 20\text{--}55$ s in this study.

Figure 4 shows the Morlet wavelet analysis results for the Insight-HXMT data at ME and ACD channels. Using the same FFT method, the long-term trend and detrended time series are separated from the raw light curves, as shown in the top and middle panels. The two main pulses are also found in the raw light curves at HXR channels (a & f), which are similar to the double main pulses measured by the LYRA from channels 1 and 2. Then the wavelet analysis technique is applied to the detrended time series, as shown in the panels (e) and (f). Thus, the quasi-periods in flare X-ray emissions can be determined in their wavelet power spectra. They both show an enhanced power over a broad range of periods at roughly 20–55 s during the flare impulsive phase, suggesting that they are multiple periods, which is similar to that in Ly α and MUV Balmer continuum emissions. Moreover, the multiple periods appear to show different lifetimes. The quasi-periods of roughly 20–40 s are found to appear between $\sim 11:56$ UT and $\sim 11:58$ UT, and they could be co-existence. While the periods of about 50–55 s are seen to occur from about 11:57 UT to 12:01 UT. That is, they are existence of multiple oscillatory signals with periods of about 20–55 s and have different lifetimes.

Figure 5 (a)–(c) presents the Morlet wavelet analysis results for the BLENWSW radio data at the low frequency of 34.75 MHz. Panels (g) & (h) plot the light curve and its detrended light curve by applying a cutoff threshold of 60 s. They both show a number of repeated and triangular peaks from about 11:57 UT to 12:02 UT, which could be regarded as the flare QPPs. Moreover, these peaks show a well one-to-one correspondence between the raw and detrended light curves, indicating that they are really QPP signals rather than the artefact of detrending. Panel (c) draws the wavelet power spectrum, which clearly shows an enhanced power over a broad range, suggesting multiple periods in the low-frequency radio flux. On the other hand, the flare QPPs with multiple

periods starts at about 11:57 UT, which are later than those begin at HXR channels, such as 1-minute time delay. Panel (d) further shows the normalized FFT power spectra of the low-frequency radio flux by applying the cutoff thresholds of 60 s (black) and 120 s (magenta) for detrending. Similar to previous LYRA results in Figure 3, the short periods of $\sim 20\text{--}55$ s can be simultaneously seen in these two FFT power spectra, and they are corresponding well with each other, although their peaks obtained from the 120-s cutoff threshold are a bit low. This confirms that the short periods are not artifacts of the detrending process.

Similar non-stationary QPPs with multiple periods can be simultaneously detected at wavelengths of $\text{Ly}\alpha$, MUV Balmer continuum, HXR and low-frequency radio during the impulsive phase of a powerful solar flare. To further study their relationship, we then draw the correlation between the HXR flux and $\text{Ly}\alpha$ emission (black), as well as the MUV Balmer continuum emission (cyan), as shown in Figure 6 (a). Here, the LYRA data has been interpolated into a time cadence of 1 s, which is same to that of the Insight-HXMT data, so that the correlation between two different instruments can be well underlined. Notice that the raw light curve rather than the detrended one is used here. The high correlation coefficients (cc.) are obtained between them, which are of 0.88 and 0.85, respectively. On the other hand, low correlation coefficients are found between the SXR flux at GOES 1–8 Å and the MUV Balmer continuum or $\text{Ly}\alpha$ emissions, i.e., coefficients of 0.12 or 0.19. These correlation coefficients further confirm that both the $\text{Ly}\alpha$ and MUV Balmer continuum emission recorded by the LYRA at channels 1 and 2 show nonthermal temporal behaviors rather than the thermal profiles, which agrees well with previous findings (e.g., Dominique et al. 2018; Milligan et al. 2020).

The time delay is found between the HXR and low-frequency radio data, as shown in Figure 1 (b). To further investigate their links, we then perform their cross-correlation analysis, as well as the cross-correlation analysis between the HXR and LYRA data, as shown in Figure 6 (b). A maximum correlation coefficient of ~ 0.57 between the HXR and low-frequency radio data is seen at the time lag of around 60 s, as indicated by the magenta vertical line, which indicates a time delay of about 60 s between them. On the other hand, the maximum correlation coefficients of 0.88 and 0.85 are found between the HXR and LYRA data at the time lag of 0 s (black vertical line), suggesting no time delay between them, which is similar to previous findings in Figure 1. We would like to state that the raw light curves rather than the detrended time series are used for the cross-correlation analysis. The maximum correlation coefficient between the HXR and radio data is only ~ 0.57 , which is slightly lower than those between HXR and LYRA data. This is because that the pulses in radio flux show large amplitudes, for instance, increasing and decaying rapidly with respect to their background emission, while the HXR/LYRA light curves only exhibit small-amplitude pulsations, as shown in Figure 1 (b). The positive correlation between the HXR and radio signals suggests that they are produced by the same process of energy releases, i.e., magnetic reconnection during the solar flare.

4. Summary and Discussion

Using the observations measured by the PROBA2/LYRA, the Insight-HXMT, and the BLENSSW, we investigate the non-stationary QPPs with multiple periods during the impulsive phase of the X9.3 flare on 2017 September 06, which was the most powerful flare of solar cycle 24. Based on the wavelet analysis technique (Torrence & Compo 1998) and the Lomb-Scargle periodogram method (Scargle 1982), the multiple periods from roughly 20 s to about 55 s are simultaneously identified during the flare impulsive phase in the Ly α emission, the MUV wavelengths around 2000 Å, as well as HXR and radio channels. Multi-mode QPPs with non-stationary properties were studied in the microwave/HXR emission during solar flares (Inglis & Nakariakov 2009; Kolotkov et al. 2015). Using the wavelet analysis method, Inglis & Nakariakov (2009) demonstrated that the multiple periods of multi-mode QPPs could be co-existed nearly simultaneously, and there was almost not significant period (or frequency) shift over time. In this study, the flare QPPs are detected simultaneously in multiple wavelengths, i.e., MUV, Ly α , HXR, and low-frequency radio. On the other hand, the multiple periods observed in this flare are not co-existing. The quasi-periods of 50–55 s are affected by the two main pulses, which makes it difficult to determine their onset time and lifetimes. However, the quasi-periods of \sim 20–40 s can only be found during \sim 11:56–11:59 UT, which are obviously shorter than the 50–55-s periods. This suggests that the multiple periods have different lifetimes. Thus, the flare QPPs observed here are regarded as multiple periods with different lifetimes. Previous studies suggested that the MUV wavelengths around 2000 Å agreed well with the hydrogen Balmer continuum emission produced in the optically thin chromosphere (Dominique et al. 2018). Therefore, this is the first report of flare-related QPPs with multiple periods in the MUV Balmer continuum emission.

The QPP behaviors of the X9.3 flare has been studied at wavelengths of radio, SXR, HXR, and even γ -ray (Kolotkov et al. 2018; Karlický & Rybák 2020; Li et al. 2020a; Zhang et al. 2021). Kolotkov et al. (2018) first investigated the QPP signals during the X9.3 flare. They found that the QPP periods varied from around 12 s to 25 s in the thermal emission during the flare impulsive and decay phases, and attributed them to be the sausage oscillations of flaring loops. Next, Li et al. (2020a) studied the flare-related QPPs with periods of about 20–30 s at channels of radio, HXR and γ -ray during the impulsive phase, and the similar periods were also reported by Zhang et al. (2021). Then, Karlický & Rybák (2020) detected multiple periods (i.e., 1–2 s, 5.3–8.5 s and 11–30 s) mainly in the radio emission during the pre-impulsive and impulsive phases of the X9.3 flare. In this study, we report the multi-periodic QPPs during the flare impulsive phase in Ly α , MUV Balmer continuum, low-frequency radio and HXR channels simultaneously. The short periods of 20–40 s are detected during \sim 11:56–11:59 UT, which are similar to previous findings in the radio, HXR and γ -ray channels (Li et al. 2020a; Zhang et al. 2021). However, they could not study the QPP behaviors after 11:59 UT, largely due to their observational limitations. Here, the long periods of \sim 50–55 s are also found from roughly 11:57 UT to 12:02 UT. We would like to point out that a much longer period of roughly 80 s could also be seen in the LYRA data, and it is mostly caused by the two main pulses during \sim 11:55:40–11:58:20 UT in the raw light curves, which are

similar to the intermittent feature in the HXR emission (Zhang et al. 2021). However, it is not suitable for a typical QPP, since it only remains two cycles (e.g., two pulses). Moreover, the flare QPPs with periods of about 60–80 s have been reported in the Ly α emission during solar flares (Li et al. 2020d). So, only the short periods between ~ 20 s and ~ 55 s are studied at wavelengths of Ly α , MUV Balmer continuum, HXR and low-frequency radio in this study.

It is necessary to discuss the generation mechanism that can be responsible for the multi-periodic QPPs detected simultaneously at wavelengths of Ly α , MUV Balmer continuum, HXR, and low-frequency radio. The Ly α irradiance during solar flare is found to be closely related with the MUV Balmer continuum emission, and it also shows highly synchronous with the HXR emission (Rubio da Costa et al. 2009; Dominique et al. 2018). On the other hand, the flare radiation in HXR and low-frequency radio channels during the impulsive phase is generally produced by the bi-directional nonthermal electrons accelerated by the magnetic reconnection (e.g., Benz 2017). Therefore, the flare QPPs simultaneously observed in the Ly α , MUV Balmer continuum, HXR and low-frequency radio channels are most likely to be triggered by a same repeated energy release process, i.e., the periodic regime of magnetic reconnection (Li et al. 2017, 2020a; Clarke et al. 2021). The pulsed, bi-directional electron beams are accelerated by the intermittent magnetic reconnection during the flare impulsive phase. The downward accelerated electrons precipitated toward the chromosphere along the flare loop, resulting in quasi-periodic enhancements in Ly α , MUV Balmer continuum and HXR emissions, while the upward electron beams escaped along an open magnetic field line and generated radio pulsations at the low frequency of 34.75 MHz. The time delay of about 60 s between the HXR QPP and the low-frequency radio QPP is attributed to the traveling time of the upward electron beams propagating outward from the Sun (Li et al. 2015; Clarke et al. 2021). It is generally accepted that the type III radio burst is produced by the electron beam traveling along the magnetic field and outwards from the Sun (Reid & Ratcliffe 2014). In particular, the radio emissions at frequencies of about 200–0.03 MHz are often dominated by the plasma emission mechanism (e.g., Gary & Hurford 1989). That is, the radio frequency (f) is roughly proportional to the local electron density (n_e), such as $f \approx 8980\sqrt{n_e}$ (e.g., Lu et al. 2017). Based on the electron density model developed by Vršnak et al. (2004), the radio flux at the frequency of 34.75 MHz is produced at the heliocentric height of roughly $2.5R_\odot$ (R_\odot represents the solar radius) above the Sun, and it agrees with previous models (e.g., Gary & Hurford 1989; Krupar et al. 2014). Then, the average speed of the electron beam is estimated to be $\sim 0.1c$ (c is the light speed), which is consistent with previous findings in the range of $0.1c$ – $0.5c$ (Dulk et al. 1987; Reid & Ratcliffe 2014; Clarke et al. 2021). Considering the multiple periods have different lifetimes, the repetitive magnetic reconnection is probably to be induced rather than spontaneous. The similar short periods have been found in the major X9.3 flare (Kolotkov et al. 2018) or in the flare Ly α emission (Van Doorselaere et al. 2011), which were interpreted in terms of sausage oscillations. Therefore, the multi-periods of ~ 20 – 55 s might be modulated by the sausage oscillations of hot plasma loops in the flare region (Chen et al. 2015; Guo et al. 2016). The flare-related QPPs with multiple periods could also be related to the length of flare loops and each other (e.g., Reznikova & Shibasaki 2011; Pugh et al. 2019). However, the other generation mechanisms, for instance, driven directly by

MHD waves, or by LRC-circuit oscillations, could not be completely ruled out, largely due to the absence of the spatially resolved information, i.e., high-resolution images at wavelengths of MUV, Ly α , radio, and HXR.

It should be stated that the Insight-HXMT is primarily used to scan the Galactic Plane and study X-ray binaries and gamma-ray bursts (Zhang et al. 2020). However, the present study reveals that it can also capture the HXR emission of solar flares, like, in this case, the X9.3 flare on 2017 September 06. The X9.3 flare was measured by the Konus-Wind in HXR and γ -ray wavelengths, but these observations only covered a total duration of about 250 s (Li et al. 2020a), which makes it impossible to study the flare-related QPPs during the whole impulsive phase. Here, using the observations recorded by the Insight-HXMT, the PROBA2/LYRA and the BLENSSW, we detect the similar flare-related QPP behaviors at channels of HXR, Ly α , MUV Balmer continuum emission, and the low-frequency radio, for instance, the multi-periods with different lifetimes. Our findings confirm the nonthermal temporal behaviors of flare radiation in Ly α and MUV Balmer continuum, which is consistent with previous observational results. In the study of Dominique et al. (2018), the derivative of the GOES SXR flux was used as a proxy for the HXR light curve, largely due to the absence of HXR measurements from solar telescopes. Thus, this study also provides an idea that some astronomical satellites such as Insight-HXMT or Fermi could also be used to study solar powerful eruptions, in particular the larger solar flare.

The authors thank the anonymous referee for his/her valuable comments and suggestions. LYRA is a project of the Centre Spatial de Liège, the Physikalisch-Meteorologisches Observatorium Davos and the Royal Observatory of Belgium funded by the Belgian Federal Science Policy Office (BELSPO) and by the Swiss Bundesamt für Bildung und Wissenschaft. This work also made use of the data from the Insight-HXMT mission, a project funded by China National Space Administration (CNSA) and the CAS. This work is supported by NSFC under grants 11973092, 12073081, 11921003, 11873095, 11790302, U1931138, U1731241, U1838202, U1838201, U1938102, U1838110, as well as CAS Strategic Pioneer Program on Space Science, Grant No. XDA15052200, and XDA15320301. D. Li is supported by the Specialized Research Fund for State Key Laboratories. The Laboratory No. 2010DP173032. The Insight-HXMT team gratefully acknowledges the support from the National Program on Key Research and Development Project (Grant No. 2016YFA0400800) from the Minister of Science and Technology of China (MOST) and the Strategic Priority Research Program of the Chinese Academy of Sciences (Grant No. XDB23040400). M. Dominique thanks the European Space Agency (ESA) and BELSPO for their support in the framework of the PRODEX Programme.

REFERENCES

Allred, J. C., Hawley, S. L., Abbett, W. P., et al. 2005, *ApJ*, 630, 573. doi:10.1086/431751

- Anfinogentov, S. A., Nakariakov, V. M., Pascoe, D. J., et al. 2021, *ApJS*, 252, 11. doi:10.3847/1538-4365/abc5c1
- Avrett, E. H., Machado, M. E., & Kurucz, R. L. 1986, *The Lower Atmosphere of Solar Flares*, 216
- Benz, A. O., Monstein, C., Meyer, H., et al. 2009, *Earth Moon and Planets*, 104, 277. doi:10.1007/s11038-008-9267-6
- Benz, A. O. 2017, *Living Reviews in Solar Physics*, 14, 2. doi:10.1007/s41116-016-0004-3
- Cao, X., Jiang, W., Meng, B., et al. 2020, *Science China Physics, Mechanics, and Astronomy*, 63, 249504. doi:10.1007/s11433-019-1506-1
- Chen, S.-X., Li, B., Xiong, M., et al. 2015, *ApJ*, 812, 22. doi:10.1088/0004-637X/812/1/22
- Clarke, B. P., Hayes, L. A., Gallagher, P. T., et al. 2021, *ApJ*, 910, 123. doi:10.3847/1538-4357/abe463
- Curdtt, W., Brekke, P., Feldman, U., et al. 2001, *A&A*, 375, 591. doi:10.1051/0004-6361:20010364
- Dennis, B. R., Tolbert, A. K., Inglis, A., et al. 2017, *ApJ*, 836, 84. doi:10.3847/1538-4357/836/1/84
- Dominique, M., Hochedez, J.-F., Schmutz, W., et al. 2013, *Sol. Phys.*, 286, 21. doi:10.1007/s11207-013-0252-5
- Dominique, M., Zhukov, A. N., Heinzel, P., et al. 2018, *ApJ*, 867, L24. doi:10.3847/2041-8213/aaeace
- Dulk, G. A., Goldman, M. V., Steinberg, J. L., et al. 1987, *A&A*, 173, 366
- Emslie, A. G., Dennis, B. R., Shih, A. Y., et al. 2012, *ApJ*, 759, 71. doi:10.1088/0004-637X/759/1/71
- Feng, S., Yu, L., Wang, F., et al. 2017, *ApJ*, 845, 11. doi:10.3847/1538-4357/aa7d52
- Feng, S., Miao, Y., Yuan, D., et al. 2020, *ApJ*, 893, L2. doi:10.3847/2041-8213/ab7dc4
- Gary, D. E. & Hurford, G. J. 1989, *Washington DC American Geophysical Union Geophysical Monograph Series*, 54, 237. doi:10.1029/GM054p0237
- Guo, M.-Z., Chen, S.-X., Li, B., et al. 2016, *Sol. Phys.*, 291, 877. doi:10.1007/s11207-016-0868-3
- Hayes, L. A., Gallagher, P. T., Dennis, B. R., et al. 2019, *ApJ*, 875, 33. doi:10.3847/1538-4357/ab0ca3
- Hayes, L. A., Inglis, A. R., Christe, S., et al. 2020, *ApJ*, 895, 50. doi:10.3847/1538-4357/ab8d40
- Heinzel, P. & Kleint, L. 2014, *ApJ*, 794, L23. doi:10.1088/2041-8205/794/2/L23

- Inglis, A. R. & Nakariakov, V. M. 2009, *A&A*, 493, 259. doi:10.1051/0004-6361:200810473
- Jing, Z., Pan, W., Yang, Y., et al. 2020, *ApJ*, 904, 41. doi:10.3847/1538-4357/abbacc
- Kashapova, L. K., Kupriyanova, E. G., Xu, Z., et al. 2020, *A&A*, 642, A195. doi:10.1051/0004-6361/201833947
- Karlický, M. & Rybák, J. 2020, *ApJS*, 250, 31. doi:10.3847/1538-4365/abb19f
- Kleint, L., Heinzel, P., Judge, P., et al. 2016, *ApJ*, 816, 88. doi:10.3847/0004-637X/816/2/88
- Kolotkov, D. Y., Nakariakov, V. M., Kupriyanova, E. G., et al. 2015, *A&A*, 574, A53. doi:10.1051/0004-6361/201424988
- Kolotkov, D. Y., Pugh, C. E., Broomhall, A.-M., et al. 2018, *ApJ*, 858, L3. doi:10.3847/2041-8213/aabde9
- Kotrč, P., Procházka, O., & Heinzel, P. 2016, *Sol. Phys.*, 291, 779. doi:10.1007/s11207-016-0860-y
- Kretzschmar, M. 2011, *A&A*, 530, A84. doi:10.1051/0004-6361/201015930
- Kupriyanova, E. G., Melnikov, V. F., Nakariakov, V. M., et al. 2010, *Sol. Phys.*, 267, 329. doi:10.1007/s11207-010-9642-0
- Kupriyanova, E., Kolotkov, D., Nakariakov, V., et al. 2020, *Solar-Terrestrial Physics*, 6, 3. doi:10.12737/stp-61202001
- Krupar, V., Maksimovic, M., Santolik, O., et al. 2014, *Sol. Phys.*, 289, 3121. doi:10.1007/s11207-014-0522-x
- Kuznetsov, A. A. & Kolotkov, D. Y. 2021, *ApJ*, 912, 81. doi:10.3847/1538-4357/abf569
- Li, D., Ning, Z. J., & Zhang, Q. M. 2015, *ApJ*, 807, 72. doi:10.1088/0004-637X/807/1/72
- Li, D., Zhang, Q. M., Huang, Y., et al. 2017, *A&A*, 597, L4. doi:10.1051/0004-6361/201629867
- Li, D., Kolotkov, D. Y., Nakariakov, V. M., et al. 2020a, *ApJ*, 888, 53. doi:10.3847/1538-4357/ab5e86
- Li, D., Feng, S., Su, W., et al. 2020b, *A&A*, 639, L5. doi:10.1051/0004-6361/202038398
- Li, B., Antolin, P., Guo, M.-Z., et al. 2020c, *Space Sci. Rev.*, 216, 136. doi:10.1007/s11214-020-00761-z
- Li, D., Lu, L., Ning, Z., et al. 2020d, *ApJ*, 893, 7. doi:10.3847/1538-4357/ab7cd1
- Li, D., 2021, *SCIENCE CHINA Technological Sciences*. In press. doi:10.1007/s11431-020-1771-7
- Liang, B., Meng, Y., Feng, S., et al. 2020, *Ap&SS*, 365, 40. doi:10.1007/s10509-020-3744-4

- Liu, C., Zhang, Y., Li, X., et al. 2020, *Science China Physics, Mechanics, and Astronomy*, 63, 249503. doi:10.1007/s11433-019-1486-x
- Lu, L., Inhester, B., Feng, L., et al. 2017, *ApJ*, 835, 188. doi:10.3847/1538-4357/835/2/188
- Lu, L., Feng, L., Li, D., et al. 2021a, *ApJS*, 253, 29. doi:10.3847/1538-4365/abd79b
- Lu, L., Li, D., Ning, Z. J., et al. 2021b, *Sol. Phys.*, accepted
- Luo, Q., Liao, J.-Y., Li, X.-F., et al. 2020, *Journal of High Energy Astrophysics*, 27, 1. doi:10.1016/j.jheap.2020.04.004
- Miao, Y., Li, D., Yuan, D., et al. 2021, *ApJ*, 908, L37. doi:10.3847/2041-8213/abdfce
- Milligan, R. O., Kerr, G. S., Dennis, B. R., et al. 2014, *ApJ*, 793, 70. doi:10.1088/0004-637X/793/2/70
- Milligan, R. O., Fleck, B., Ireland, J., et al. 2017, *ApJ*, 848, L8. doi:10.3847/2041-8213/aa8f3a
- Milligan, R. O., Hudson, H. S., Chamberlin, P. C., et al. 2020, *Space Weather*, 18, e02331. doi:10.1029/2019SW002331
- Nakariakov, V. M., Foullon, C., Myagkova, I. N., et al. 2010, *ApJ*, 708, L47. doi:10.1088/2041-8205/708/1/L47
- Nakariakov, V. M., Anfinogentov, S., Storozhenko, A. A., et al. 2018, *ApJ*, 859, 154. doi:10.3847/1538-4357/aabfb9
- Nakariakov, V. M., Kolotkov, D. Y., Kupriyanova, E. G., et al. 2019, *Plasma Physics and Controlled Fusion*, 61, 014024. doi:10.1088/1361-6587/aad97c
- Nakariakov, V. M. & Kolotkov, D. Y. 2020, *ARA&A*, 58, 441. doi:10.1146/annurev-astro-032320-042940
- Ning, Z., Ding, M. D., Wu, H. A., et al. 2005, *A&A*, 437, 691. doi:10.1051/0004-6361:20041944
- Ning, Z. 2014, *Sol. Phys.*, 289, 1239. doi:10.1007/s11207-013-0405-6
- Ning, Z. 2017, *Sol. Phys.*, 292, 11. doi:10.1007/s11207-016-1037-4
- Nusinov, A. A., Kazachevskaya, T. V., Kuznetsov, S. N., et al. 2006, *Solar System Research*, 40, 282. doi:10.1134/S0038094606040034
- Pugh, C. E., Broomhall, A.-M., & Nakariakov, V. M. 2019, *A&A*, 624, A65. doi:10.1051/0004-6361/201834455
- Reid, H. A. S. & Ratcliffe, H. 2014, *Research in Astronomy and Astrophysics*, 14, 773. doi:10.1088/1674-4527/14/7/003

- Reeves, K. K., Polito, V., Chen, B., et al. 2020, *ApJ*, 905, 165. doi:10.3847/1538-4357/abc4e0
- Reznikova, V. E. & Shibasaki, K. 2011, *A&A*, 525, A112. doi:10.1051/0004-6361/201015600
- Rubio da Costa, F., Fletcher, L., Labrosse, N., et al. 2009, *A&A*, 507, 1005. doi:10.1051/0004-6361/200912651
- Samanta T., Tian H., Chen B., et al. 2021, *The Innovation*, 2(1), 100083. doi:10.1016/j.xinn.2021.100083
- Scargle, J. D. 1982, *ApJ*, 263, 835. doi:10.1086/160554
- Shen, Y.-D., Liu, Y., Su, J.-T., et al. 2013, *Sol. Phys.*, 288, 585. doi:10.1007/s11207-013-0395-4
- Shen, Y., Tang, Z., Li, H., et al. 2018, *MNRAS*, 480, L63. doi:10.1093/mnrasl/sly127
- Shen, Y., Chen, P. F., Liu, Y. D., et al. 2019, *ApJ*, 873, 22. doi:10.3847/1538-4357/ab01dd
- Srivastava, A. K., Zaqarashvili, T. V., Uddin, W., et al. 2008, *MNRAS*, 388, 1899. doi:10.1111/j.1365-2966.2008.13532.x
- Tan, B., Zhang, Y., Tan, C., et al. 2010, *ApJ*, 723, 25. doi:10.1088/0004-637X/723/1/25
- Tan, B., Yu, Z., Huang, J., et al. 2016, *ApJ*, 833, 206. doi:10.3847/1538-4357/833/2/206
- Tan, B.-L., Yan, Y., Li, T., et al. 2020, *Research in Astronomy and Astrophysics*, 20, 090. doi:10.1088/1674-4527/20/6/90
- Thurgood, J. O., Pontin, D. I., & McLaughlin, J. A. 2017, *ApJ*, 844, 2. doi:10.3847/1538-4357/aa79fa
- Tian, H., Young, P. R., Reeves, K. K., et al. 2016, *ApJ*, 823, L16. doi:10.3847/2041-8205/823/1/L16
- Torrence, C. & Compo, G. P. 1998, *Bulletin of the American Meteorological Society*, 79, 61. doi:10.1175/1520-0477(1998)079;0061:APGTWA;2.0.CO;2
- Wang, T., Ofman, L., Yuan, D., et al. 2021, *Space Sci. Rev.*, 217, 34. doi:10.1007/s11214-021-00811-0
- Van Doorselaere, T., De Groof, A., Zender, J., et al. 2011, *ApJ*, 740, 90. doi:10.1088/0004-637X/740/2/90
- Vaughan, S. 2005, *A&A*, 431, 391. doi:10.1051/0004-6361:20041453
- Vršnak, B., Magdalenić, J., & Zlobec, P. 2004, *A&A*, 413, 753. doi:10.1051/0004-6361:20034060
- Woods, T. N., Kopp, G., & Chamberlin, P. C. 2006, *Journal of Geophysical Research (Space Physics)*, 111, A10S14. doi:10.1029/2005JA011507

- Xue, J., Su, Y., Li, H., et al. 2020, *ApJ*, 898, 88. doi:10.3847/1538-4357/ab9a3d
- Yu, S. & Chen, B. 2019, *ApJ*, 872, 71. doi:10.3847/1538-4357/aaff6d
- Yuan, D., Feng, S., Li, D., et al. 2019, *ApJ*, 886, L25. doi:10.3847/2041-8213/ab5648
- Zimovets, I. V., McLaughlin, J. A., Srivastava, A. K., et al. 2021, *Space Sci. Rev.*, 217, 66. doi:10.1007/s11214-021-00840-9
- Zhang, S.-N., Li, T., Lu, F., et al. 2020, *Science China Physics, Mechanics, and Astronomy*, 63, 249502. doi:10.1007/s11433-019-1432-6
- Zhang, P., Wang, W., Su, Y., et al. 2021, arXiv:2106.09506

This preprint was prepared with the AAS L^AT_EX macros v5.2.

Table 1: The details of observational instruments in this study.

Instruments	Channels	Cadence	Wavelengths	Bandpass
LYRA	Channel 1	0.05 s	1200–1230 Å	Ly α
	Channel 2	0.05 s	1900–2220 Å	MUV
	Channel 4	0.05 s	1–200 Å	SXR/EUV
GOES-16	XRS	1 s	1–8 Å	SXR
	ME	1 s	5–30 keV	SXR/HXR
HXMT	ACD	1 s	>100 keV	HXR
BLENSW		0.25 s	~20–76 MHz	Radio

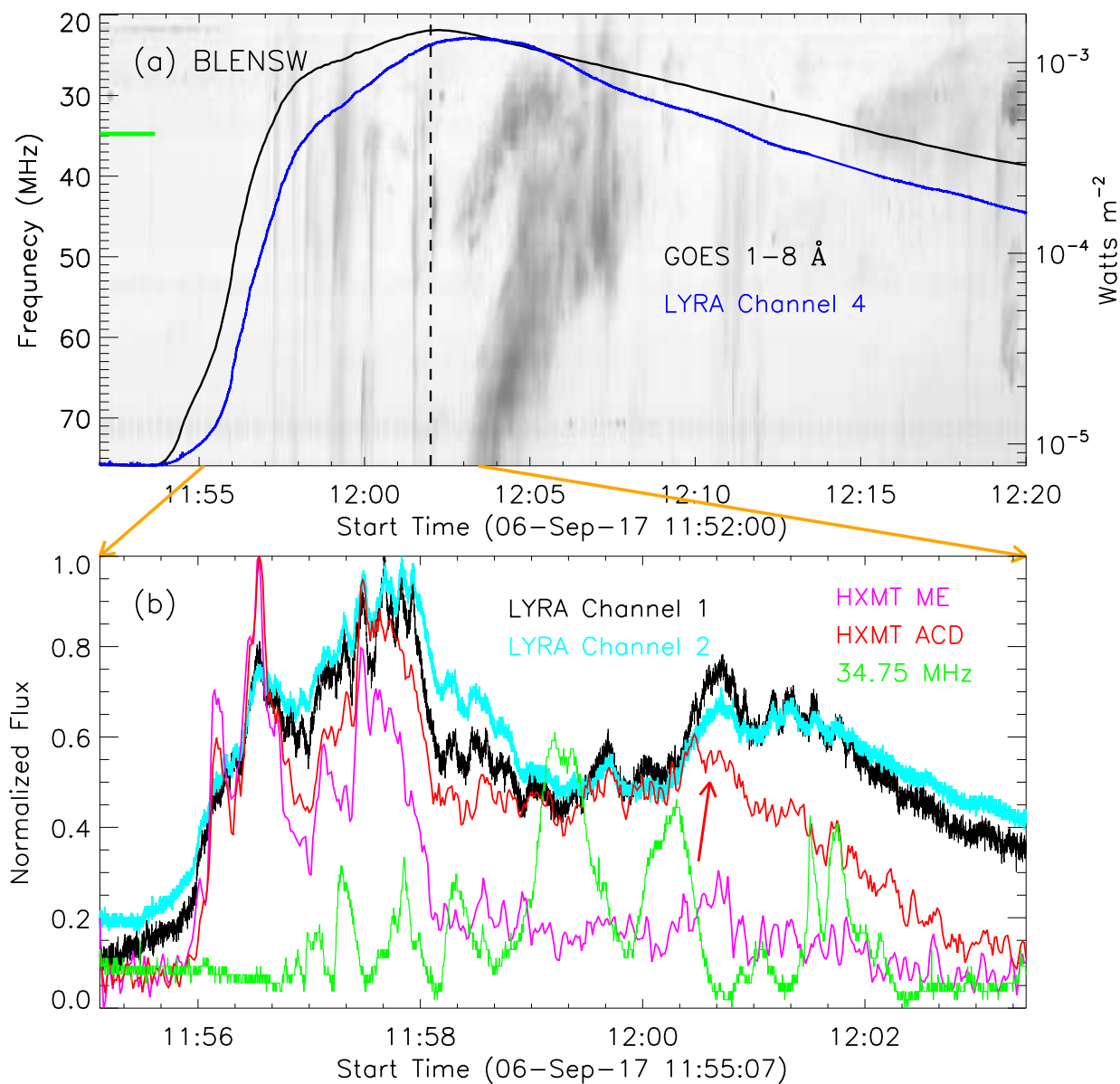


Fig. 1.— Light curves integrated over the whole Sun during the X9.3 flare on 2017 September 06, recorded by the GOES, the LYRA, the Insight-HXMT, and the BLENSSW, respectively. Notice that, all the light curves except for the GOES flux are shown as normalized. The context image in panel (a) is the radio dynamic spectra measured by the BLENSSW. The short green line marks the radio frequency at 34.75 MHz, which is plotted in panel (b), the dashed line indicates the flare peak time.

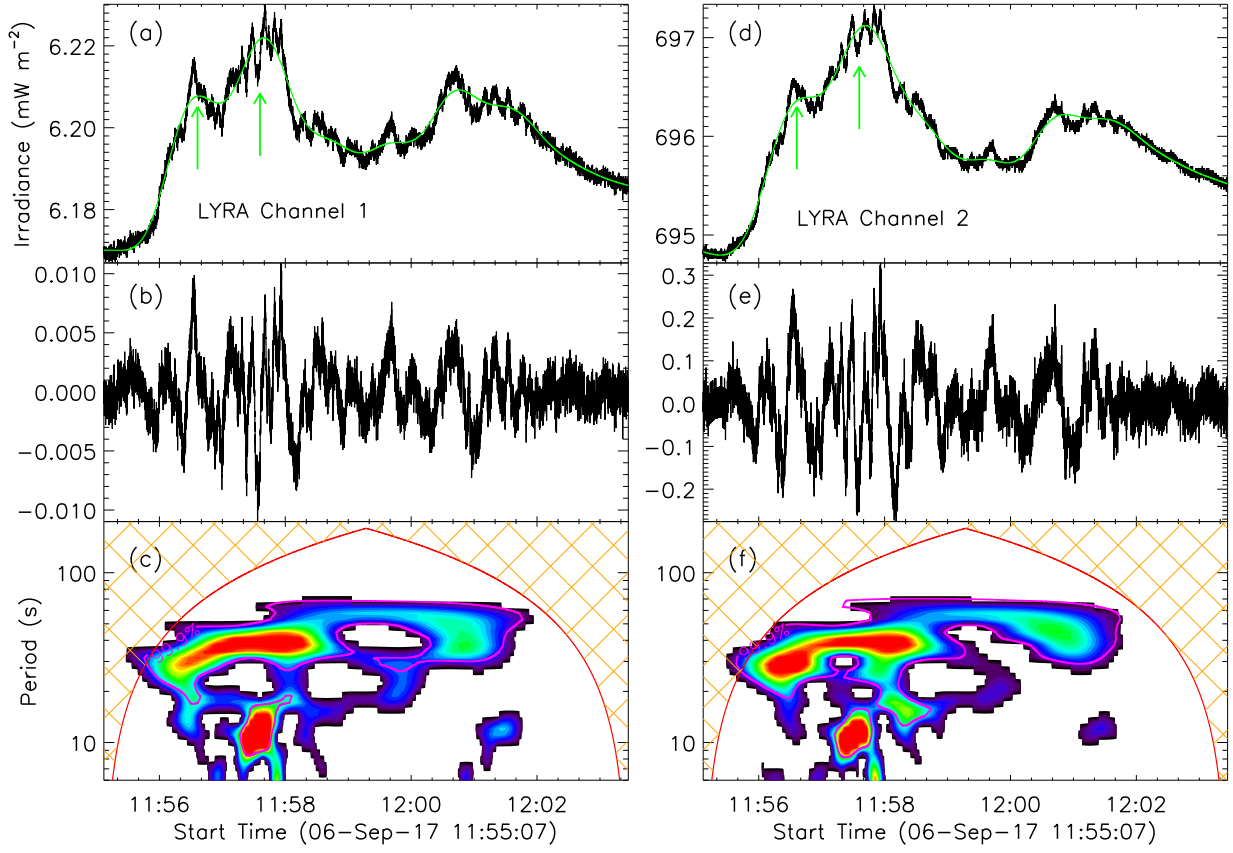


Fig. 2.— Panels (a) & (d): Full-disk light curves (black) observed by LYRA at channels 1 and 2, and their FFT filtered profiles (green). Two green arrows marked the double main peaks in the raw light curves. Panels (b) & (e): detrended light curves. Panels (c) & (f): Morlet wavelet power spectra. The magenta lines outline the significance level of 99.9%.

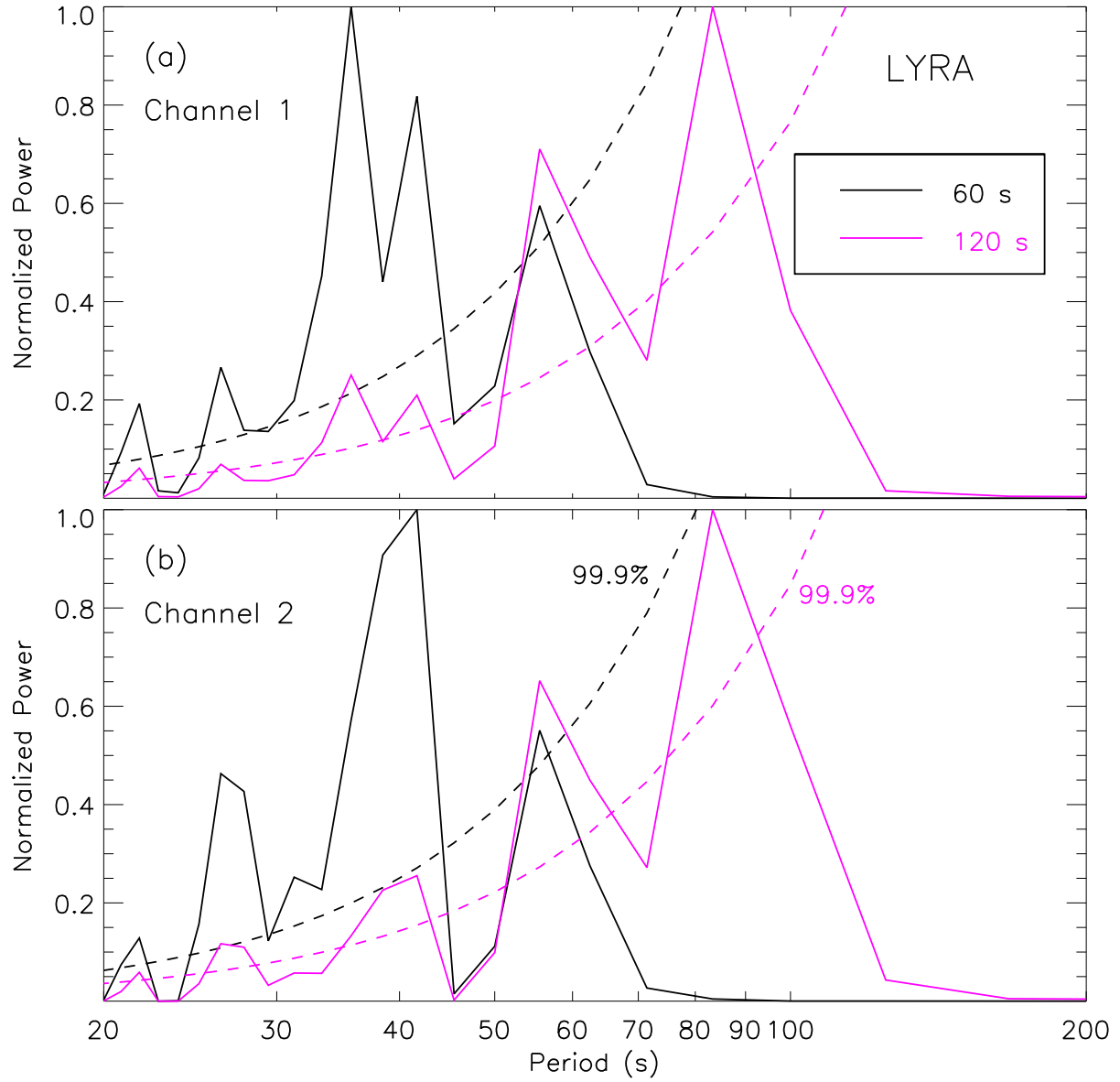


Fig. 3.— FFT power spectra derived from the LYRA at channels 1 (a) and 2 (b). The detrended light curves obtained from the cutoff periods at 60 s (black) and 120 s (magenta), respectively. Their significance levels are marked by the dashed lines.

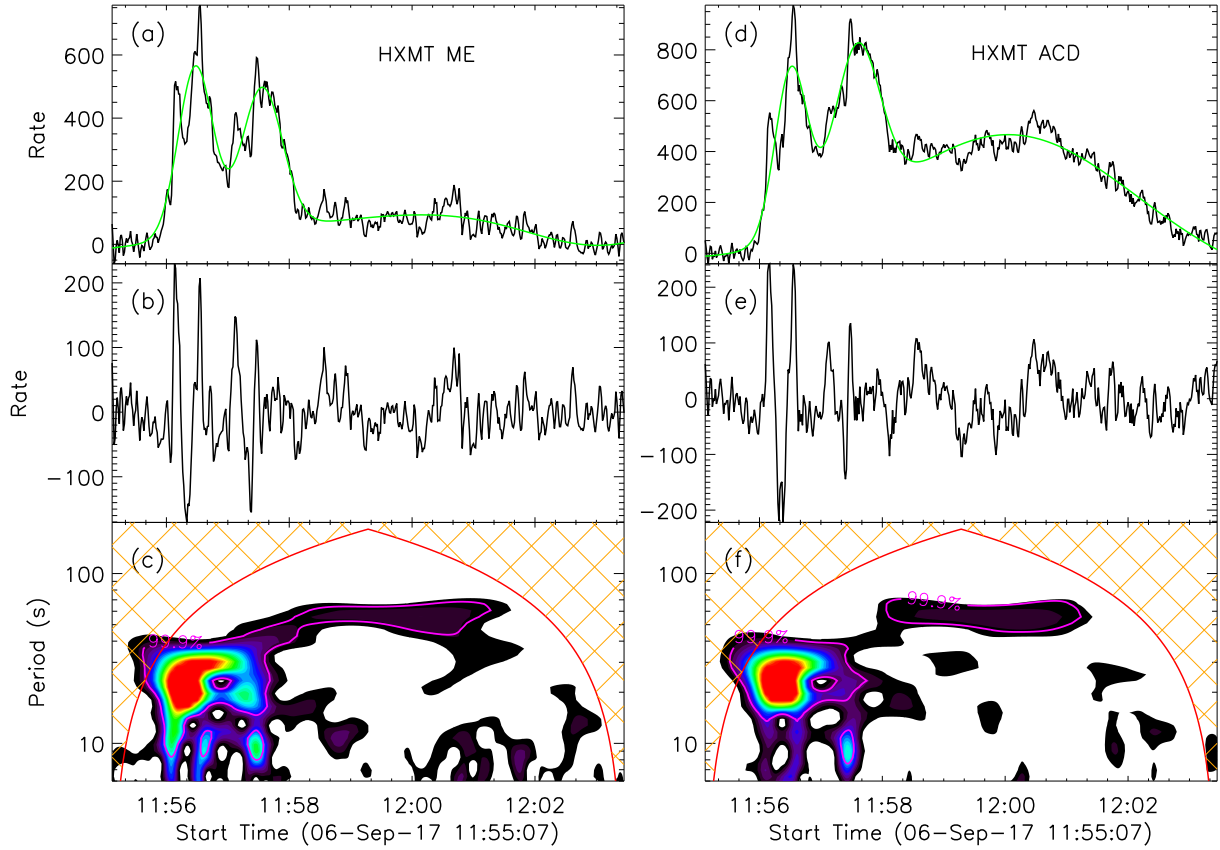


Fig. 4.— Panel (a), (d): Full-disk light curves (black) observed by the HXMT ME and ACD (black), as well as their FFT filtered profiles (green). Panels (b), (e): detrended light curve. Panels (c), (f): Morlet wavelet power spectra. The magenta lines outline the significance level of 99.9%.

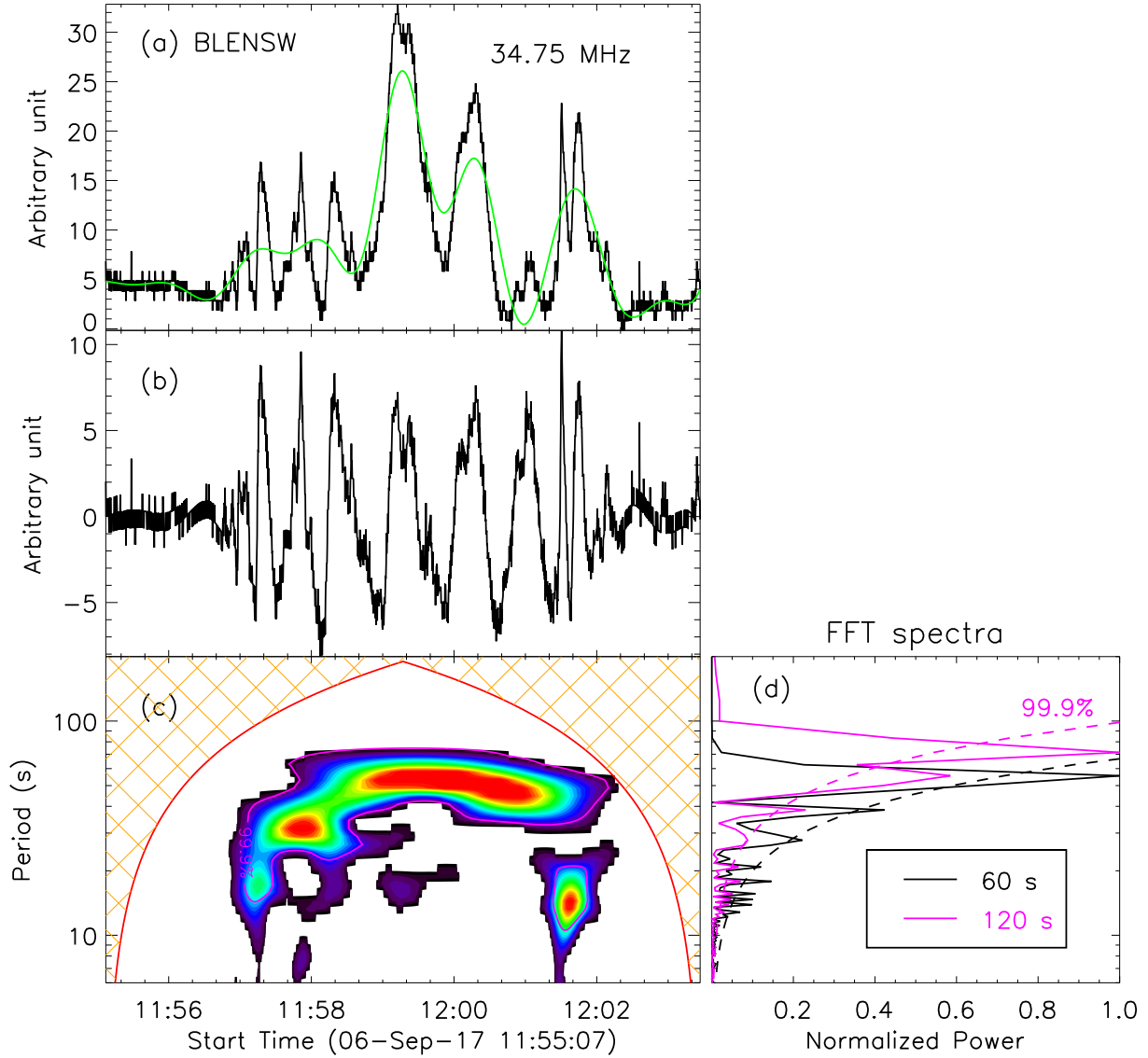


Fig. 5.— Panel (a): Full-disk light curves (black) observed by the BLENWS at a frequency of 34.75 MHz (black), and its FFT filtered profile (green). Panels (b): detrended light curve. Panels (c): Morlet wavelet power spectra. The magenta lines outline the significance level of 99.9%. Panel (d): FFT power spectra of the detrended light curves with cutoff periods of 60 s (black) and 120 s (magenta), respectively. While their significance levels are marked by the dashed lines.

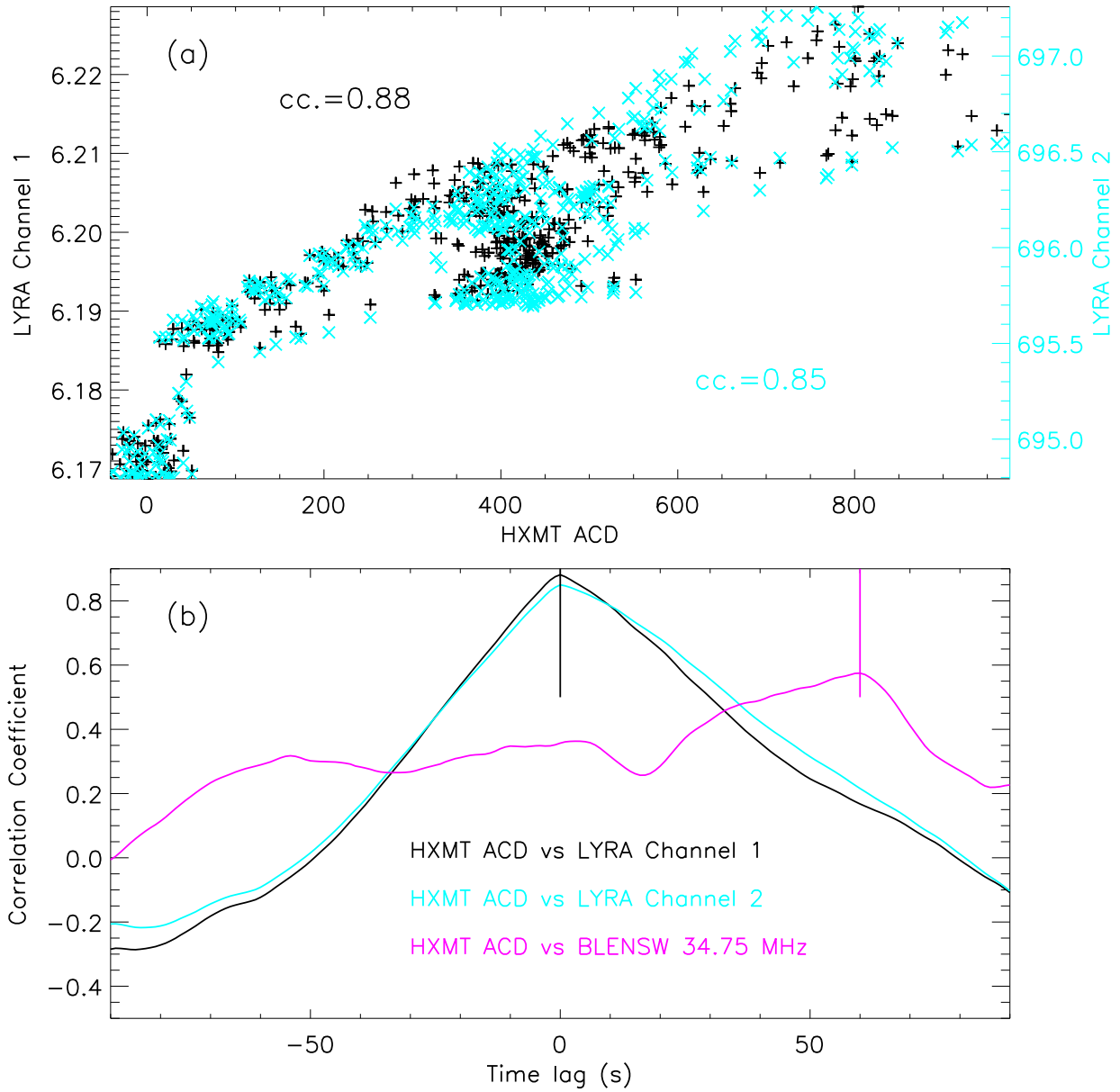


Fig. 6.— Pane (a): $\text{Ly}\alpha$ and MUV Balmer continuum emissions depend on the HXR flux during the impulsive phase of solar flare, i.e., between $\sim 11:55$ UT and $\sim 12:03$ UT. The correlation coefficients (cc.) are given. Panel (b): Cross-correlation analysis results, which respect to the raw light curves at HXMT ACD.

A. Appendix

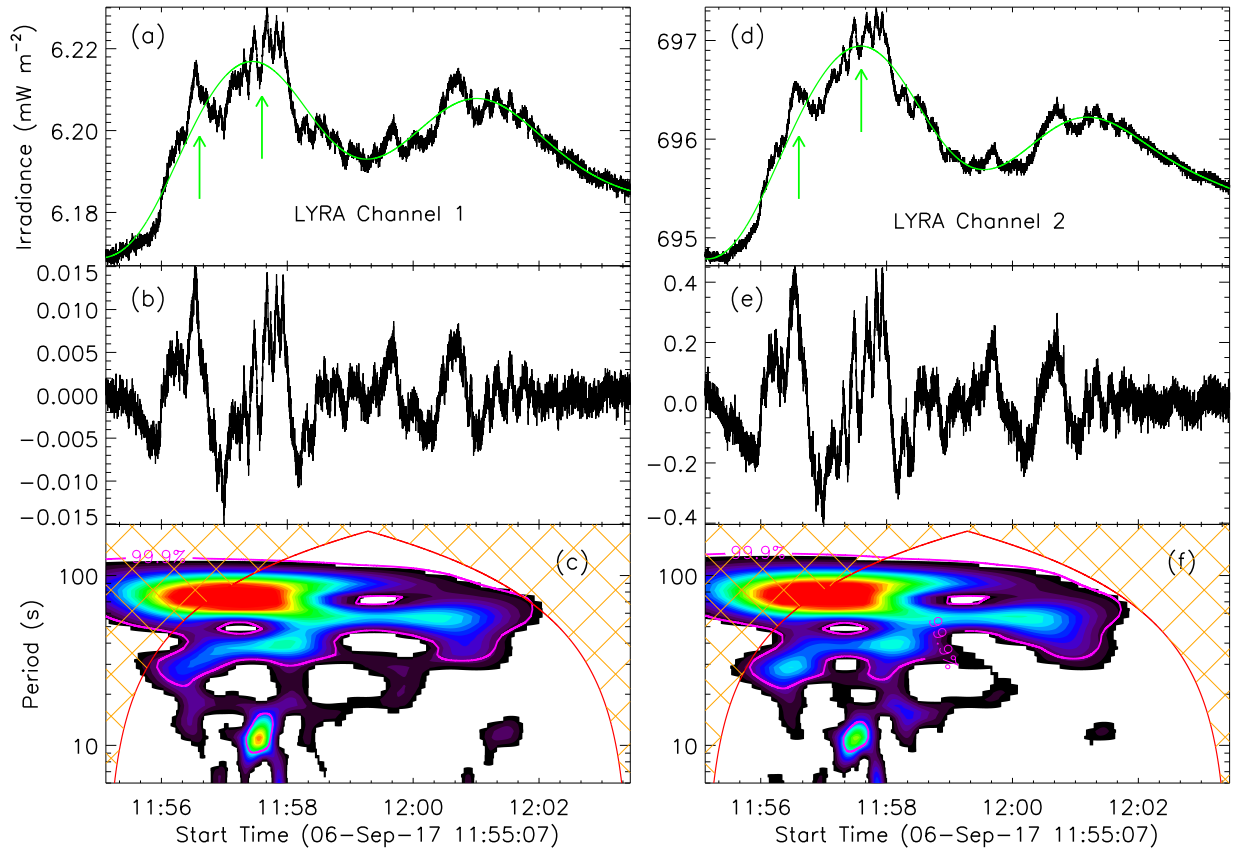


Fig. A.— Following in Figure 2, the Morlet wavelet analysis results for the LYRA data. Here, the detrending signals and their wavelet power spectra are obtained from the cutoff period of 120 s. The magenta lines outline the significance level of 99.9%.